

Motion-Invariant Variational Auto-Encoding of Brain Structural Connectomes

Yizi Zhang*, Meimei Liu†, Zhengwu Zhang‡, David Dunson§

Abstract

Mapping of human brain structural connectomes via diffusion MRI offers a unique opportunity to understand brain structural connectivity and relate it to various human traits, such as cognition. However, the presence of motion artifacts during image acquisition can compromise the accuracy of connectome reconstructions and subsequent inference results. We develop a generative model to learn low-dimensional representations of structural connectomes that are invariant to motion artifacts, so that we can link brain networks and human traits more accurately, and generate motion-adjusted connectomes. We applied the proposed model to data from the Adolescent Brain Cognitive Development (ABCD) study and the Human Connectome Project (HCP) to investigate how our motion-invariant connectomes facilitate understanding of the brain network and its relationship with cognition. Empirical results demonstrate that the proposed motion-invariant variational auto-encoder (inv-VAE) outperforms its competitors in various aspects. In particular, motion-adjusted structural connectomes are more strongly associated with a wide array of cognition-related traits than other approaches without motion adjustment. Open source code is available at <https://github.com/yzhang511/inv-vae>¹.

1 Introduction

To comprehensively understand brain function and organization, enormous efforts have been dedicated to constructing the *brain structural connectome*, defined as a collection of white matter fiber tracts connecting different brain regions. Recent advances in non-invasive neuroimaging techniques have resulted in a rapid proliferation of brain imaging datasets, e.g., the Human Connectome Project (HCP) [1], and the Adolescent Brain Cognitive Development (ABCD) study [2]. Inspired by these developments, an immense literature [3, 4] focuses on the analysis of structural connectomes recovered from diffusion-weighted magnetic resonance imaging (dMRI) data. However, these studies often face challenges in how to handle subject head movement during image acquisition. Head motion often results in image misalignment and

*Yizi Zhang, Department of Statistics, Columbia University (e-mail: yz4123@columbia.edu).

†Meimei Liu, Department of Statistics, Virginia Polytechnic Institute and State University.

‡Zhengwu Zhang, Department of Statistics and Operations Research, The University of North Carolina at Chapel Hill.

§David Dunson, Department of Statistical Science, Duke University.

¹This work is licensed under a Creative Commons Attribution 4.0 International License. For more details please see <https://creativecommons.org/licenses/by/4.0/>

introduces artifacts in the data that prevent accurate connectome reconstructions [5]. Correction for these biases is essential to statistical analysis of connectomes, motivating us to develop novel statistical methods that can model and analyze brain structural connectomes in an invariant manner [6, 7].

Our goal is to learn a low-dimensional representation of brain connectomes invariant to motion artifacts, facilitating prediction and inference on the relationship between brain structure and cognitive abilities. In the neuroimaging literature, one commonly used method to improve data quality is registering images corrupted by motion to a geometrically correct template [8, 9]. However, in dMRI, head motion can cause location change or signal dropout, introducing significant difficulties in registration [10]. Alternative motion correction methods seek to remove or replace outliers in a diffusion dataset, relying on various outlier detection metrics [11, 12]. This approach is inadequate as it might discard important information, especially when the amount of data available is limited. Also, simply discarding outlying observations in the input data does not correct the impact of motion on downstream analyses should there be residual artifacts left unadjusted. Therefore, our major motivation is to develop a method that adjusts for motion in the process of modeling instead of data preprocessing.

In biomedical imaging, removing spurious effects in high dimensional data has been an important problem for at least the last decade. Without proper adjustment, the association between the signal of interest and one or more nuisance variables can degrade the ability to infer the signal accurately. This problem is particularly salient in brain imaging studies, and various tools have been developed. A popular matrix factorization method [13] uses a singular value decomposition of the original matrix to filter out the singular vector associated with the nuisance variable, and reconstructs an adjusted matrix with the remaining singular vectors. Similarly, the Sparse Orthogonal to Group (SOG) procedure [14] creates an adjusted dataset based on a constrained form of matrix decomposition. In addition, model-based methods are popular alternatives for removing unwanted associations in the data. For example, distance-weighted discrimination [15] adapts Support Vector Machines (SVM) for batch effect removal; the ComBat method [16] adjusts for batch effects in data using empirical Bayes. Our work falls under the model-based framework, and we are particularly interested in incorporating batch effect removal into a deep learning framework so that the non-linear batch effect can be modeled and removed.

Removing unwanted information in the deep learning literature is formulated as an invariant representation learning problem. Existing deep learning methods learn invariant representations in an adversarial way. [17] developed convolutional neural networks to correct motion-corrupted images by augmenting L_1 loss with adversarial loss. Another example of adversarial invariance is learning a split representation of data through competitive training between the prediction task and a reconstruction task coupled with disentanglement [18]. However, blind spots in adversarial training can lead to poor performance in test data due to the curse of dimensionality and the scarcity of training data [19]. To bypass adversarial training, we propose to learn invariant representations with information theory-based algorithmic

fairness [20]. Our method removes the mutual information between latent representations and subject motion, where latent representations are learned via graph variational auto-encoders (VAE).

We aim to model brain connectomes with motion adjusted and learn their representations invariant to arbitrary nuisance factors. We find that structural connectome data are strongly affected by motion artifacts even after performing motion correction with *eddy* (a tool for correcting eddy currents and movements in dMRI) [21]. Our analyses of the ABCD and HCP data suggest that individuals with large head movement during data acquisition have fewer reconstructed fiber connections than those without in almost all brain regions. Therefore, we develop a generative model to learn the distribution of brain connectomes with motion adjusted, and learn low-dimensional representations of structural connectomes that are invariant to head motion. Motion invariance is achieved by introducing a penalized VAE objective to remove the mutual information between connectome representations and head motion. Code is available at <https://github.com/yzhang511/inv-vae>. The learned invariant representation can facilitate our understanding of the impact of motion on structural connectivity reconstructions, and can be used to produce motion-adjusted connectomes for any downstream analysis tasks, including prediction of behavior- and cognition-related traits, and inferring structural connections between brain regions. We further link the invariant representation to human traits to better understand the relationship between human connectomes and cognition. Our experiments show that motion-invariant representations improve prediction of many cognitive traits compared to connectome representations without motion adjustment.

2 Datasets Studied

2.1 Structural Connectomes and Cognitive Traits

The ABCD study tracks the brain development of over 10,000 adolescents in the United States. We downloaded and processed the diffusion MRI (dMRI) data for 8,646 subjects from the NIH Data Archive. Details about data acquisition and preprocessing can be found in [22]. The Human Connectome Project (HCP) characterizes brain connectivity in more than 1,000 adults; see [23] for details about data acquisition. The latest dMRI data from the HCP can be accessed through ConnectomeDB. We downloaded and processed 1065 subjects from the HCP.

To extract structural connectomes from the raw dMRI data, a reproducible tractography algorithm [24] was used to generate the whole-brain tractography for each subject. We used the Desikan-Killiany parcellation [25] to define brain regions of interest (ROIs) corresponding to different nodes in the brain network in Fig. 1 (A). The Desikan-Killiany atlas contains 68 ROIs with 34 ROIs belonging to each hemisphere. We used Freesurfer [26] to perform brain registration and parcellation. Fig. 1 illustrates the tractography data and the brain parcellation, from which we extracted streamlines connecting ROI pairs. Fiber count is often used as a measure of the coupling strength between ROI pairs in the current

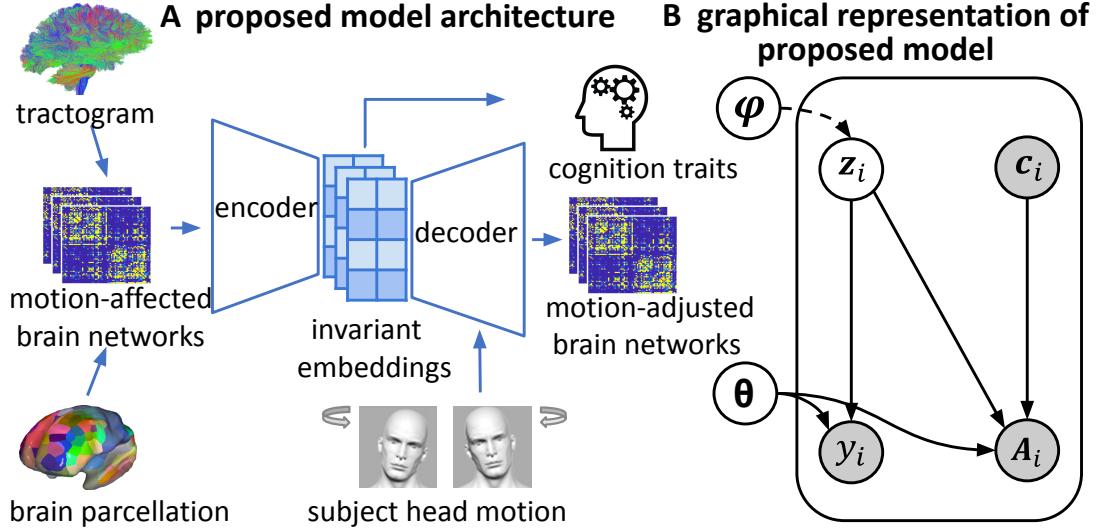


Figure 1: (A) Connectome extraction and the proposed model architecture. Structural brain networks are obtained from tractography and brain parcellation, and are affected by motion artifacts. With adjustment for head motion, invariant embeddings learned by the VAE model can generate motion-adjusted brain networks, and can be linked to cognition-related traits. (B) Graphical representation of the proposed model. The generative model assumes that individual i 's brain network, A_i , is generated from a latent z_i and motion c_i . Trait y_i only depends on z_i not on c_i . Observed variables are colored in gray. The inference model is marked by the dashed line, whereas the generative model is marked by the solid line. ϕ and θ are parameters of the inference and generative model, respectively.

literature [27, 4], and therefore we summarized each brain connection with its fiber count to generate the brain networks.

Both ABCD and HCP use reliable measures to assess a wide range of human behaviors and functions [28]. We focus on inferring the relationship between structural connectomes and cognition-related traits, e.g., scores from the picture vocabulary and oral reading recognition tests.

2.2 Motion Quantification

Neuroimaging studies collect multiple image frames for each subject during data acquisition. The first image frame acquired serves as a reference frame, so that other frames can be aligned to the reference frame to obtain framewise displacement. Motion measurements include translational and rotational displacements. In our analysis, we only consider $b = 0$ dMRI data (non-diffusion weighted). In the ABCD data, each individual has 7 $b = 0$ frames spreading evenly during the diffusion scanning. Each HCP subject has 18 $b = 0$ frames. We computed the average translational and rotational displacements over all frames for each individual, which were used to represent the amount of head motion. Fig. 2 (A) shows distributions of subject motion standardized to the 0-1 range in both datasets.

We explicitly adjusted for subject motion in the proposed model; see Section 3. To explore the impact of translation and rotation on structural connectomes, we assigned individuals into a large and a small motion group corresponding to each movement type. Fig. 2 shows the cutoff lines for translation and motion, respectively, for both ABCD and HCP data. Specifically, in the ABCD data, individuals whose

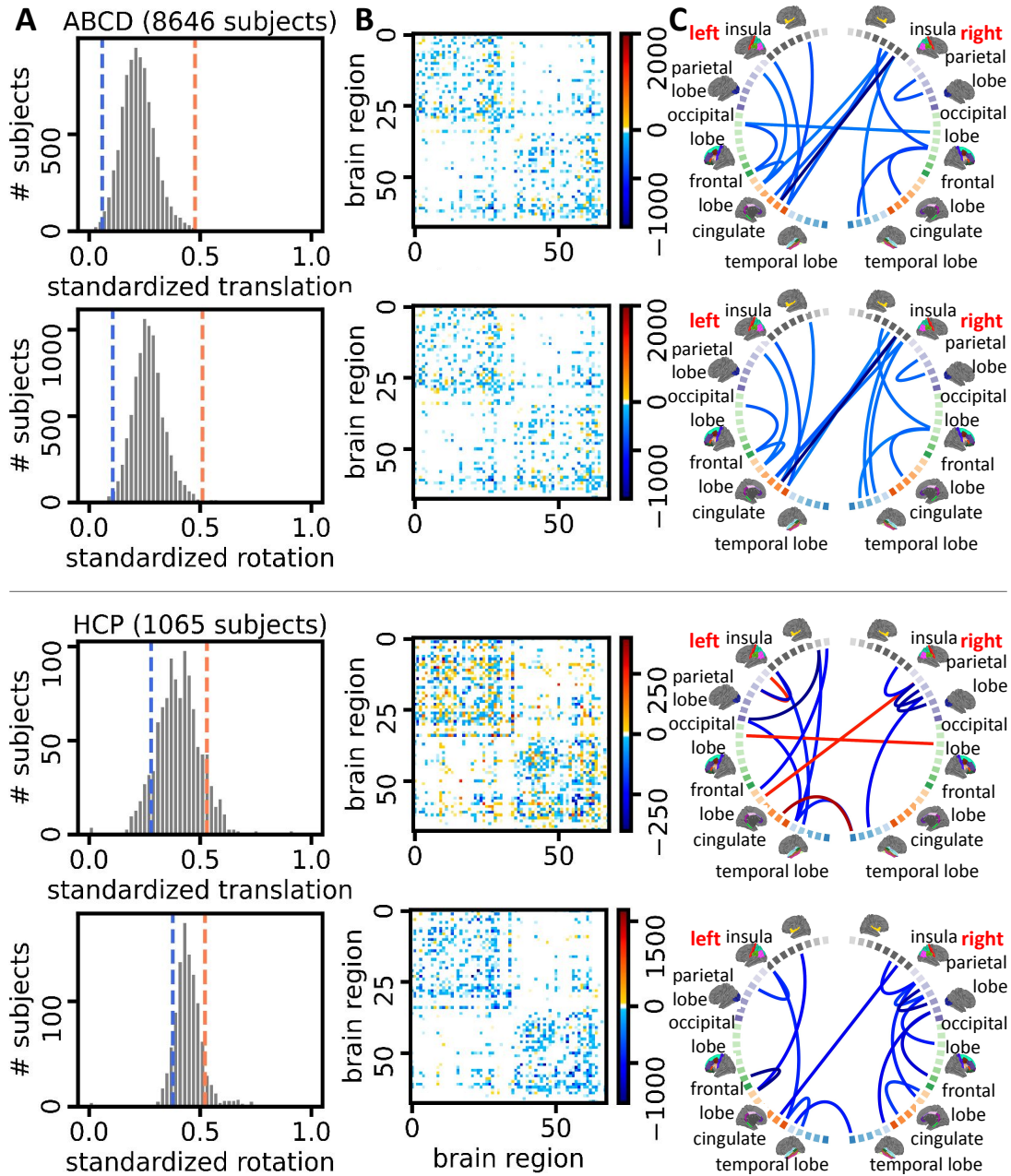


Figure 2: (A) Distributions of subject translation and rotation standardized to the 0-1 range in the ABCD and HCP data. For ABCD subjects, log transformation is applied to adjust for skewed data before standardization. In ABCD data, the 1st and 99-th percentiles are marked by the blue and orange lines. In HCP data, the blue and orange lines indicate the 10-th and 90-th percentiles. Subjects whose standardized motions fall below the blue line are assigned to the small motion group, and those falling above the orange line are in the large motion group. (B) Differences of mean networks between the large and small (large – small) motion groups. (C) Plotting column (B) in circular plots. The color scale is the same as that in (B), but we only show 15 edges with the largest fiber count differences for display.

translations were ranked among the top (bottom) 1 percent were assigned to the large (small) motion group; the same applies to rotation. In the HCP data, we used the top and the bottom 10 percent as the threshold. We then quantify brain connection differences between groups. We subtracted edge-specific means of the small motion group from those of the large motion group and show the results as adjacency matrices in Fig. 2 (B). In addition, we visualized between-group differences using a circular layout in Fig. 2 (C) to examine how connection patterns and strength differ across ROIs. Note that the dMRI data used here are preprocessed with the FSL eddy tool and its motion correction procedures. Fig. 2 (B, C) reveal that large motion subjects have fewer apparent fiber connections than small motion subjects in almost all ROIs, implying that motion artifacts still affect structural connection reconstruction even after motion correction in the preprocessing stage [5, 21].

Interestingly, rotation has a larger impact than translation on structural connections in the HCP data, whereas translation and rotation have similar impacts in the ABCD data. Motivated by these findings, we propose the motion-invariant graph variational auto-encoder in Section 3 to remove such systematic motion artifacts from the connectome data and downstream analyses.

3 Method

The brain connectome for an individual is represented as an undirected graph $\mathcal{G} = (\mathcal{V}, \mathcal{E})$ with nodes \mathcal{V} and edges \mathcal{E} . The collection of nodes \mathcal{V} refers to the partitioned brain regions, and the set of edges \mathcal{E} represents connections between pairs of ROIs. The ROIs are pre-aligned so that each node in \mathcal{V} corresponds to the same brain region across different subjects. We use the symmetric adjacency matrix \mathbf{A} to represent \mathcal{G} with A_{uv} denoting the number of streamlines connecting ROIs u and v ; $A_{uu} = 0$ since we don't consider self-connections. For N subjects, we denote the network data as $\mathbf{A}_i, i = 1, 2, \dots, N$. Also, denote the cognitive trait score for an individual as y_i , and the amount of head motion as \mathbf{c}_i . We set $\mathbf{c}_i \in \mathbb{R}^C$ as a vector with each dimension measuring different aspects of motion like the amount of translation or rotation. We average the motions across all image frames and standardize each movement type to the 0-1 range to ensure that they are on the same scale.

We aim to infer the relationship between individuals' structural connectomes recovered from neuroimaging data and their measured cognition traits, while adjusting for motion artifacts introduced in data acquisition. The key to achieving this goal is to learn a low-dimensional feature representation of \mathbf{A}_i as \mathbf{z}_i that is invariant to motion \mathbf{c}_i , then relate the feature \mathbf{z}_i to y_i . Inspired by the variational auto-encoder (VAE) framework in [29], we achieve our goal through three steps: 1) an encoder module (inference model) that learns the mapping from the observation \mathbf{A}_i to the motion-invariant latent variable \mathbf{z}_i ; 2) a decoder module (generative model) that specifies how to construct \mathbf{A}_i from \mathbf{z}_i and motion \mathbf{c}_i , and 3) a regression module to link the motion-invariant \mathbf{z}_i to the cognition trait y_i ; see Fig. 1 for

the model architecture and the corresponding graphical model. In the following sections, we start with introducing our graph generative model and then discuss the encoder and regression modules.

3.1 Brain Network Generative Model

For each individual i , we assume the edges $A_{i[uv]}$ are conditionally independent given \mathbf{z}_i and \mathbf{c}_i . The likelihood of the set of edges in \mathbf{A}_i is

$$p_{\boldsymbol{\theta}}(\mathbf{A}_i | \mathbf{z}_i, \mathbf{c}_i) = \prod_{u=1}^V \prod_{v=1}^V p_{\boldsymbol{\theta}}(A_{i[uv]} | \mathbf{z}_i, \mathbf{c}_i), \quad (1)$$

where $p_{\boldsymbol{\theta}}(\mathbf{A}_i | \mathbf{z}_i, \mathbf{c}_i)$ is the generative model for \mathbf{A}_i given \mathbf{z}_i and \mathbf{c}_i , parameterized by $\boldsymbol{\theta}$ learned via neural networks. We assume \mathbf{A}_i to be generated from the following process:

$$\mathbf{z}_i \sim \mathcal{N}(\mathbf{0}, \mathbf{I}_K), \quad (2)$$

$$A_{i[uv]} | (\mathbf{z}_i, \mathbf{c}_i) \sim \text{Pois}(\lambda_{i[uv]}(\mathbf{z}_i, \mathbf{c}_i)), \quad (3)$$

where K is the dimension of the latent feature space. The fiber count between ROIs u and v is modeled using a Poisson distribution with a parameter $\lambda_{i[uv]}(\mathbf{z}_i, \mathbf{c}_i)$, which relates to both the encoded feature \mathbf{z}_i and motion \mathbf{c}_i .

To capture the varying effect of motion across individuals and brain connections, we further model $\lambda_{i[uv]}(\mathbf{z}_i, \mathbf{c}_i)$ as

$$\tilde{\mathbf{z}}_i := \mathbf{z}_i \oplus \mathbf{c}_i, \quad (4)$$

$$\lambda_{i[uv]}(\mathbf{z}_i, \mathbf{c}_i) = \exp(\xi_{uv} + \psi_{uv}(\tilde{\mathbf{z}}_i)), \quad (5)$$

where \oplus denotes the concatenation operator, and $\tilde{\mathbf{z}}_i \in \mathbb{R}^{K+C}$ is a concatenated vector representing motion-affected latent features. ξ_{uv} is a baseline parameter controlling the population connection strength between regions u and v , representing shared structural similarity across individuals, and $\psi_{uv}(\tilde{\mathbf{z}}_i)$ characterizes individual connection strength after accounting for motion.

We model $\psi_{uv}(\tilde{\mathbf{z}}_i)$ based on the latent space model in [30]. The key idea is that the connection strength (fiber count) between regions u and v depends on their distance in some network latent space in \mathbb{R}^R . In this network latent space, each brain region is represented by a vector in the \mathbb{R}^R space, with the distance between two points reflecting the degree of association between the corresponding brain regions. The closer two points are in this space, the stronger their connection is expected to be. The network latent space is different from the latent space of $\tilde{\mathbf{z}}_i$, which represents a low-dimensional space where the original high-dimensional brain structural connectomes are encoded into a lower-dimensional

representation.

We construct a mapping \mathbf{X} from \mathbb{R}^{K+C} to $\mathbb{R}^{V \times R}$ that maps the motion-affected feature $\tilde{\mathbf{z}}_i$ to the network latent space that captures the latent positions of all brain regions, i.e., $\mathbf{X}(\tilde{\mathbf{z}}_i)^\top = (\mathbf{X}_1(\tilde{\mathbf{z}}_i), \dots, \mathbf{X}_V(\tilde{\mathbf{z}}_i))$ with $\mathbf{X}_u(\tilde{\mathbf{z}}_i) = (X_{u1}(\tilde{\mathbf{z}}_i), \dots, X_{uR}(\tilde{\mathbf{z}}_i))^\top \in \mathbb{R}^R$ for brain region u . Specifically, we assume each node $u \in \mathcal{V}$ for individual i lies in a latent space \mathbb{R}^R and represent $\psi_{uv}(\tilde{\mathbf{z}}_i)$ as

$$\psi_{uv}(\tilde{\mathbf{z}}_i) = \sum_{r=1}^R \alpha_r X_{ur}(\tilde{\mathbf{z}}_i) X_{vr}(\tilde{\mathbf{z}}_i), \quad (6)$$

where $\alpha_r > 0$ is a weight controlling the importance of the r -th dimension. A large positive inner product between $\mathbf{X}_u(\tilde{\mathbf{z}}_i)$ and $\mathbf{X}_v(\tilde{\mathbf{z}}_i)$ implies a large fiber count between this ROI pair. Therefore, $\mathbf{X}_u(\tilde{\mathbf{z}}_i)$ incorporates the geometric collaborations among nodes, and broadcasts the impact of motion to all brain connections. [31] proposed a graph convolutional network (GCN) to learn a nonlinear mapping from the encoded feature \mathbf{z}_i to $(\mathbf{X}_1(\mathbf{z}_i), \dots, \mathbf{X}_V(\mathbf{z}_i))$, leveraging on unique geometric features of the brain networks. The same procedure is adopted in this paper with the additional adjustment for motion \mathbf{c}_i , and we defer the detailed GCN framework to Appendix A.

3.2 Motion Invariant Brain Network Encoding and Traits Prediction

We are interested in studying the relationship between brain structural networks and human traits, correcting for the effect of motion in data acquisition. The key is to find an optimal encoder that produces \mathbf{z}_i from \mathbf{A}_i invariant to \mathbf{c}_i , and then formulate a regression of the trait y_i with respect to the latent feature vector \mathbf{z}_i . We represent the inference model (encoder) as $q_\phi(\mathbf{z}_i | \mathbf{A}_i)$, the generative model (decoder) as $p_\theta(\mathbf{A}_i | \mathbf{z}_i, \mathbf{c}_i)$, and regression as $p_\theta(y_i | \mathbf{z}_i)$. Our invariant encoding and trait prediction task is to find $q_\phi(\mathbf{z}_i | \mathbf{A}_i)$ and $p_\theta(\mathbf{A}_i | \mathbf{z}_i, \mathbf{c}_i)$ that maximize $\mathbb{E}_{\mathbf{A}_i, y_i, \mathbf{c}_i} [\log p_\theta(\mathbf{A}_i, y_i | \mathbf{c}_i)]$, subject to \mathbf{z}_i being independent of \mathbf{c}_i . Here $p_\theta(\mathbf{A}_i, y_i | \mathbf{c}_i)$ is the joint likelihood of \mathbf{A}_i, y_i conditional on \mathbf{c}_i . Statistical independence is based on random variables having zero correlation. Since correlation is a limited notion of statistical dependence, which does not capture non-linear dependencies, we instead use mutual information between \mathbf{z}_i and \mathbf{c}_i to quantify their dependency similar to [20], and formulate the objective function as follows:

$$\mathcal{L}(\mathbf{A}_i, y_i, \mathbf{c}_i; \theta, \phi) = \mathbb{E}_{\mathbf{A}_i, y_i, \mathbf{c}_i} [\log p_\theta(\mathbf{A}_i, y_i | \mathbf{c}_i)] - \lambda I(\mathbf{z}_i, \mathbf{c}_i), \quad (7)$$

where $I(\mathbf{z}_i, \mathbf{c}_i)$ is the mutual information between \mathbf{z}_i and \mathbf{c}_i , and λ is a trade-off parameter between the joint likelihood and the mutual information. ϕ are parameters of the encoder that are learned via neural networks.

To simplify our model, we assume 1) the human trait y_i and the brain connectivity \mathbf{A}_i are condition-

ally independent given the latent representation \mathbf{z}_i for individual i , and 2) only \mathbf{A}_i is affected by \mathbf{c}_i so y_i is not affected. Assumption 2) indicates that motion happens randomly given the population considered and does not relate to the human traits (e.g., cognitive ability) considered. In certain scenarios, this assumption might not hold. For example, in the older population, people with mild cognitive impairment (MCI) tend to move more than normal controls [32], and if y_i is an indicator of MCI, Assumption 2) does not hold here. Assumption 1) indicates that the encoded feature \mathbf{z}_i contains all the information from \mathbf{A}_i needed to predict y_i , and the residuals are independent of each other. Intuitively, we assume the motion \mathbf{c}_i explains part of the variability in brain networks \mathbf{A}_i , but this part of variability in \mathbf{A}_i does not relate to y_i . Of course, we can modify our model to add \mathbf{c}_i into the prediction of y_i in the case that \mathbf{c}_i is not independent of y_i . But it will make the final results difficult to interpret since we are mostly concerned with the relationship between \mathbf{A}_i and y_i .

Under Assumptions 1) and 2), we can express the conditional likelihood of \mathbf{A}_i, y_i given \mathbf{c}_i as

$$\log p_{\theta}(\mathbf{A}_i, y_i | \mathbf{c}_i) \geq \mathbb{E}_{\mathbf{z}_i \sim q_{\phi}}[\log p_{\theta}(\mathbf{A}_i | \mathbf{z}_i, \mathbf{c}_i) + \log p_{\theta}(y_i | \mathbf{z}_i)] - KL[q_{\phi}(\mathbf{z}_i | \mathbf{A}_i) || p(\mathbf{z}_i)]. \quad (8)$$

The derivation is based on Jensen’s inequality; see Appendix B. Intuitively, the lower bound of $\log p_{\theta}(\mathbf{A}_i, y_i | \mathbf{c}_i)$ in (8) consists of three parts. The first term, $\log p_{\theta}(\mathbf{A}_i | \mathbf{z}_i, \mathbf{c}_i)$, is a reconstruction error that utilizes log-likelihood to measure how well the generative model in (3) reconstructs \mathbf{A}_i . The second term, $\log p_{\theta}(y_i | \mathbf{z}_i)$, measures the trait prediction accuracy. The third KL divergence term is a regularizer that pushes $q_{\phi}(\mathbf{z}_i | \mathbf{A}_i)$ to be close to its prior $\mathcal{N}(\mathbf{0}, \mathbf{I}_K)$ so that we can sample \mathbf{z}_i easily.

For the second term in the objective function (7), we can upper bound $I(\mathbf{z}_i, \mathbf{c}_i)$ as

$$I(\mathbf{z}_i, \mathbf{c}_i) \leq \mathbb{E}_{\mathbf{A}_i}[KL[q_{\phi}(\mathbf{z}_i | \mathbf{A}_i) || q_{\phi}(\mathbf{z}_i)]] - \mathbb{E}_{\mathbf{A}_i, \mathbf{c}_i, \mathbf{z}_i \sim q_{\phi}}[\log(\mathbf{A}_i | \mathbf{z}_i, \mathbf{c}_i)], \quad (9)$$

which consists of two parts: the KL divergence between $q_{\phi}(\mathbf{z}_i | \mathbf{A}_i)$ and its marginal $q_{\phi}(\mathbf{z}_i)$ to ensure less variability across the input data \mathbf{A}_i , and the reconstruction error. See Appendix C for detailed derivations of (9).

Combining the log-likelihood and the mutual information terms, our training objective in (7) can be expressed as

$$\begin{aligned} \mathcal{L}(\mathbf{A}_i, y_i, \mathbf{c}_i; \theta, \phi) &= \mathbb{E}_{\mathbf{A}_i, y_i, \mathbf{c}_i}[\log p_{\theta}(\mathbf{A}_i, y_i | \mathbf{c}_i)] - \lambda I(\mathbf{z}_i, \mathbf{c}_i) \\ &\geq -\mathbb{E}_{\mathbf{A}_i, y_i, \mathbf{c}_i} \left[KL \left[q_{\phi}(\mathbf{z}_i | \mathbf{A}_i) || p(\mathbf{z}_i) \right] + \lambda KL \left[q_{\phi}(\mathbf{z}_i | \mathbf{A}_i) || q_{\phi}(\mathbf{z}_i) \right] \right] \\ &\quad - (1 + \lambda) \mathbb{E}_{\mathbf{z}_i \sim q_{\phi}}[\log p_{\theta}(\mathbf{A}_i | \mathbf{z}_i, \mathbf{c}_i)] + \log p_{\theta}(y_i | \mathbf{z}_i) \end{aligned} \quad (10)$$

Our goal is to maximize $\mathcal{L}(\mathbf{A}_i, y_i, \mathbf{c}_i; \theta, \phi)$ through its lower bound (10). In practice, the expectation

in (10) is intractable and we employ Monte Carlo approximation for computation; see Appendix D. We define the approximated objective as $\tilde{\mathcal{L}}(\mathbf{A}_i, y_i, \mathbf{c}_i; \boldsymbol{\theta}, \phi)$, and implement a stochastic variational Bayesian Algorithm 1 to update the parameters using mini-batch training. For the regression module, we consider $p_{\boldsymbol{\theta}}(y_i | \mathbf{z}_i)$ as a univariate Gaussian, i.e., $y_i \sim \mathcal{N}(\mathbf{z}_i^\top \boldsymbol{\beta} + b, \sigma^2)$, where $\boldsymbol{\beta}, b, \sigma^2 \in \boldsymbol{\theta}$ are parameters to be learned. We list the model parameters and architecture in the Appendix E.

Algorithm 1 Motion-Invariant Variational Auto-Encoders

Input: $\{\mathbf{A}_i\}_{i=1}^N, \{y_i\}_{i=1}^N, \{\mathbf{c}_i\}_{i=1}^N$.

Initialize $\boldsymbol{\theta}, \phi$

while not converged **do**

 Sample a batch of $\{\mathbf{A}_i\}_{i=1}^m$, denoted as \mathcal{A}_m .

for all $\mathbf{A}_i \in \mathcal{A}_m$ **do**

 Sample $\epsilon_i \in \mathcal{N}(\mathbf{0}, \mathbf{I}_K)$.

 Compute $\mathbf{z}_i = \boldsymbol{\mu}_\phi(\mathbf{A}_i) + \epsilon_i \odot \boldsymbol{\Sigma}_\phi(\mathbf{A}_i)$.

 Compute the gradients $\nabla_{\boldsymbol{\theta}} \tilde{\mathcal{L}}(\mathbf{A}_i, y_i, \mathbf{c}_i; \boldsymbol{\theta}, \phi)$
 and $\nabla_{\phi} \tilde{\mathcal{L}}(\mathbf{A}_i, y_i, \mathbf{c}_i; \boldsymbol{\theta}, \phi)$ with \mathbf{z}_i .

end for

 Average the gradients across the batch.

 Update $\boldsymbol{\theta}, \phi$ using gradients of $\boldsymbol{\theta}, \phi$.

end while

Return $\boldsymbol{\theta}, \phi$.

4 Simulation Study

We first conducted a simulation study to verify the efficacy of our method in removing unwanted information from the data. We simulated random graphs with the community structure [33] using the Python package *NetworkX*. Random graphs of two communities were considered: Nodes in the same group are connected with a probability of 0.25, and nodes of different groups are connected with a probability of 0.01. We simulated 1,000 such networks $\{\mathbf{A}_i\}_{i=1}^n$, where $\mathbf{A}_i \in \mathbb{R}^{V \times V}$ with $V = 68$ nodes and $n = 1,000$. Fig. 3 (A) displays the average network across 1,000 simulated networks. Next, we simulated a *nuisance* variable, $\{s_i\}_{i=1}^n$, by sampling 20% of its elements from $\mathcal{N}(0.6, 0.05)$ and the rest from $\mathcal{N}(1, 0.01)$. We generated the nuisance-affected networks $\tilde{\mathbf{A}}_i$ by propagating s_i across all edges in \mathbf{A}_i as follows:

$$\tilde{\mathbf{A}}_i = (s_i \mathbf{A}_i)^\top (s_i \mathbf{A}_i). \quad (11)$$

Intuitively, $s_i \sim \mathcal{N}(0.6, 0.05)$ introduces large artifacts, since its multiplication with \mathbf{A}_i in (11) results in a $\tilde{\mathbf{A}}_i$ with reduced edge values; $s_i \sim \mathcal{N}(1, 0.01)$ generates small artifacts as the multiplication operation in (11) changes the edges of \mathbf{A}_i to a lesser extent. The average network across 1,000 such nuisance-affected networks is displayed in Fig. 3 (A). To visualize the impact of the simulated nuisance variable, the edge-specific differences of the large and small nuisance groups are computed for both simulated networks $\{\mathbf{A}_i\}_{i=1}^n$ and nuisance-affected networks $\{\tilde{\mathbf{A}}_i\}_{i=1}^n$ (Fig. 3 (B)). We observe apparent differences

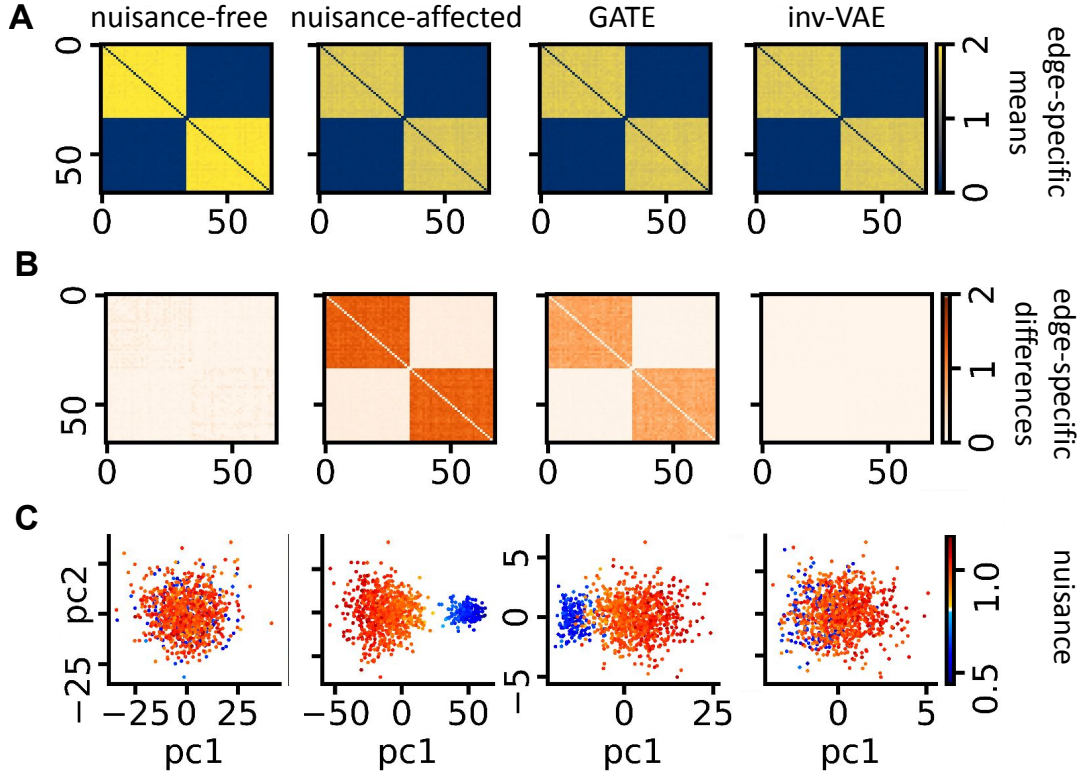


Figure 3: **(A)** Edge-specific means of simulated networks, nuisance-affected networks, reconstructed networks by GATE and nuisance-corrected networks by inv-VAE. **(B)** Edge-specific differences between networks affected by large and small nuisance artifacts. The order of plots follows that in **(A)**. **(C)** PCA projections of simulated networks, nuisance-affected networks, latent embeddings learned by GATE, and invariant embeddings from inv-VAE colored by the amount of nuisance artifacts.

in edge values between the large and small nuisance groups of $\{\tilde{\mathbf{A}}_i\}_{i=1}^n$. We further applied principal component analysis (PCA) to both $\{\mathbf{A}_i\}_{i=1}^n$ and $\{\tilde{\mathbf{A}}_i\}_{i=1}^n$, and visualized their projections onto the first two principal components (PCs) in Fig. 3 **(C)**. The first two PCs of $\{\mathbf{A}_i\}_{i=1}^n$ are indistinguishable. Note that these simulated networks are nuisance-free, even though we colored their projections with the simulated nuisance for visualization purposes. On the contrary, we observe an apparent separation between the large and small nuisance groups of $\{\tilde{\mathbf{A}}_i\}_{i=1}^n$ after introducing unwanted associations between the nuisance variable and the simulated networks.

To demonstrate the effectiveness of our method in removing artifacts introduced by the nuisance variable, we further compared inv-VAE with the graph auto-encoder (GATE) developed in [31]. GATE has the same generative model as inv-VAE (see Section 3) except without adjusting for \mathbf{c}_i . Specifically, GATE assumes the following generative process for the brain network \mathbf{A}_i :

$$\begin{aligned}
 A_{i[uv]} | \mathbf{z}_i &\sim \text{Poisson}\left(\lambda_{i[uv]}(\mathbf{z}_i)\right), \quad \mathbf{z}_i \sim \mathcal{N}(\mathbf{0}, \mathbf{I}_K), \\
 \lambda_{i[uv]}(\mathbf{z}_i) &= \exp(\xi_{uv} + \psi_{uv}(\mathbf{z}_i)), \\
 \psi_{uv}(\mathbf{z}_i) &= \sum_{r=1}^R \alpha_r X_{ur}(\mathbf{z}_i) X_{vr}(\mathbf{z}_i).
 \end{aligned} \tag{12}$$

Moreover, GATE learns the latent vector \mathbf{z}_i using the following objective

$$\mathcal{L}(\mathbf{A}_i, y_i; \boldsymbol{\theta}, \phi) = \mathbb{E}_{\mathbf{z}_i \sim q_\phi} [\log p_{\boldsymbol{\theta}}(y_i | \mathbf{z}_i)] + \mathbb{E}_{\mathbf{z}_i \sim q_\phi} [\log p_{\boldsymbol{\theta}}(\mathbf{A}_i | \mathbf{z}_i)] - KL[q_\phi(\mathbf{z}_i | \mathbf{A}_i) || p_{\boldsymbol{\theta}}(\mathbf{z}_i)] \quad (13)$$

instead of the motion-invariant objective in (10). We trained GATE using $\{\tilde{\mathbf{A}}_i\}_{i=1}^n$ to learn latent representations of nuisance-affected networks. The learned latents were used by the generative model in (12) to reconstruct networks in Fig. 3 (A). Fig. 3 (B) and (C) show the reconstructed edge-specific differences between the large and small nuisance group, and the first two PCs of the learned latent variables, respectively.

Next, we trained inv-VAE with $\{\tilde{\mathbf{A}}_i\}_{i=1}^n$ to learn parameters ϕ and $\boldsymbol{\theta}$ for the inference and generative model. The inference model then learned motion-invariant latent representations, from which the generative model produced nuisance-corrected networks (Fig. 3 (A)) by setting $s_i = 1$. As previously defined, $s_i \approx 1$ corresponds to small nuisance artifacts, whereas a small s_i represents large nuisance artifacts. This is because multiplication of \mathbf{A}_i with a small s_i in (11) shrinks its edge values to a large degree, whereas multiplication with $s_i \approx 1$ keeps the edge values roughly unchanged. Between-group edge-specific differences of the nuisance-corrected networks, and the first two PCs of invariant latents are shown in Fig. 3 (B, C). Fig. 3 (B, C) together suggest that GATE reconstructed the artifacts introduced by the nuisance variable, and its learned latent embeddings were affected by nuisance artifacts. On the contrary, such edge-specific differences between the large and small nuisance groups do not exist in the nuisance-corrected networks from inv-VAE, and projections of invariant embeddings of the large and small nuisance groups are indistinguishable. This observation implies that inv-VAE has the ability to remove unwanted information from the data.

5 Applications to the ABCD and HCP Data

5.1 Understanding and Removing Motion Artifacts

We applied our inv-VAE to the ABCD (8,646 subjects) and HCP data (1065 subjects). A major motivation of our work is to understand how motion affects learning a low-dimensional representation of the structural connectome and to remove motion artifacts from the connectome data. To this end, we compared inv-VAE to its competitors on two tasks: 1) learning a latent connectome representation that is uninformative of motion; 2) generating a motion-adjusted connectome.

We first averaged the *motion-affected brain network* \mathbf{A}_i over all individuals in the study and obtained the *motion-affected edge-specific means* (see Section 2.2) of the ABCD and HCP datasets, respectively. We call the resulting matrices as “motion-affected”, meaning no motion adjustment has been done. Fig. 4-5 (A) show the motion-affected edge-specific means in both datasets. We assigned subjects into a

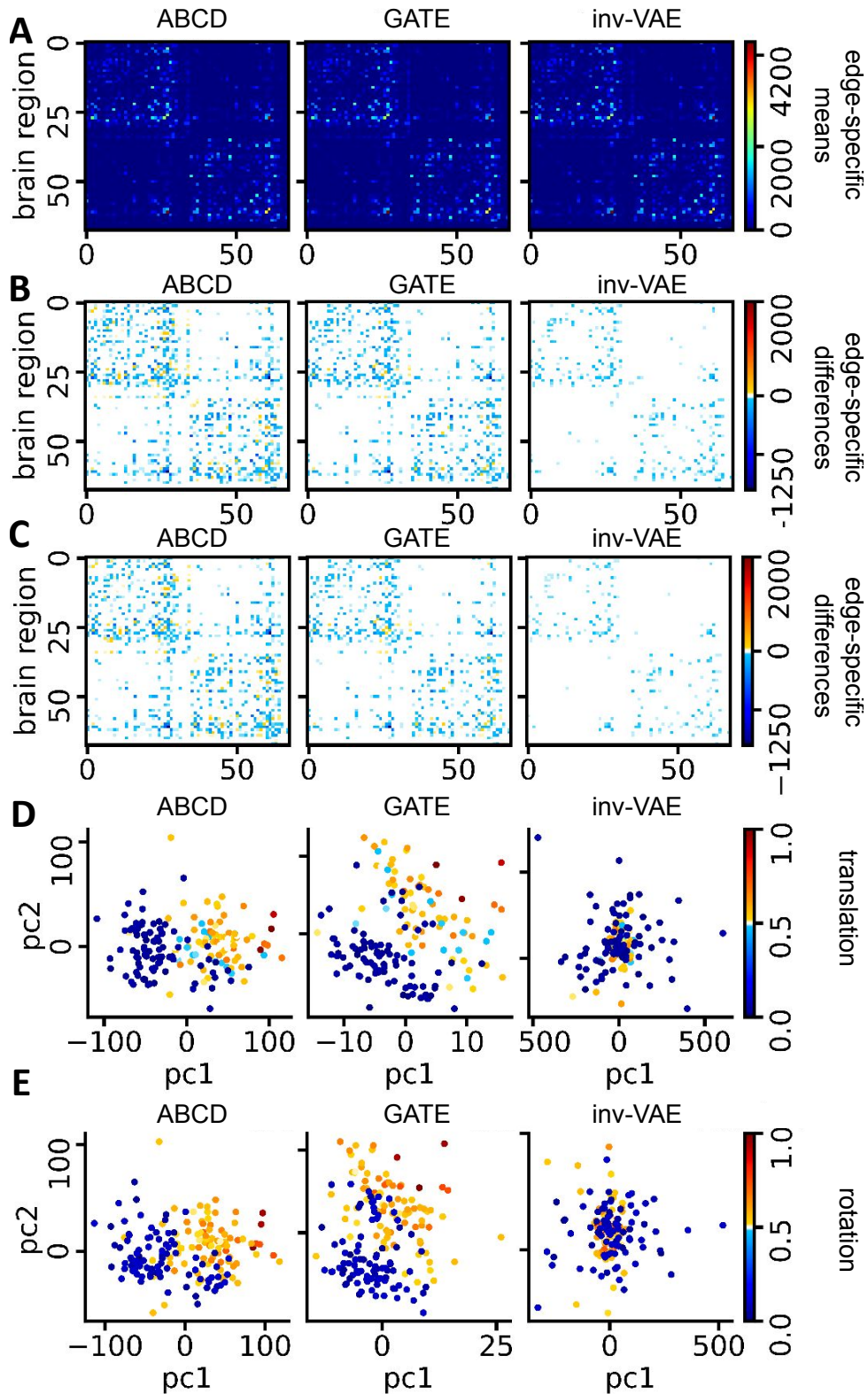


Figure 4: (A) From left to right: observed edge-specific means of ABCD brain networks, reconstructed brain networks by GATE, and motion-adjusted brain networks by inv-VAE, color-coded by fiber count. (B) and (C): edge-specific differences (large group subtract small group) for translation and rotation respectively, colored by differences in fiber count. Ordering follows that in (A). (D) and (E): from left to right - the first two PC scores of ABCD brain networks, latent embeddings learned by GATE, and invariant embeddings from inv-VAE for observations in the large and small-motion groups, colored by the amount of translation (D) and rotation (E) respectively.

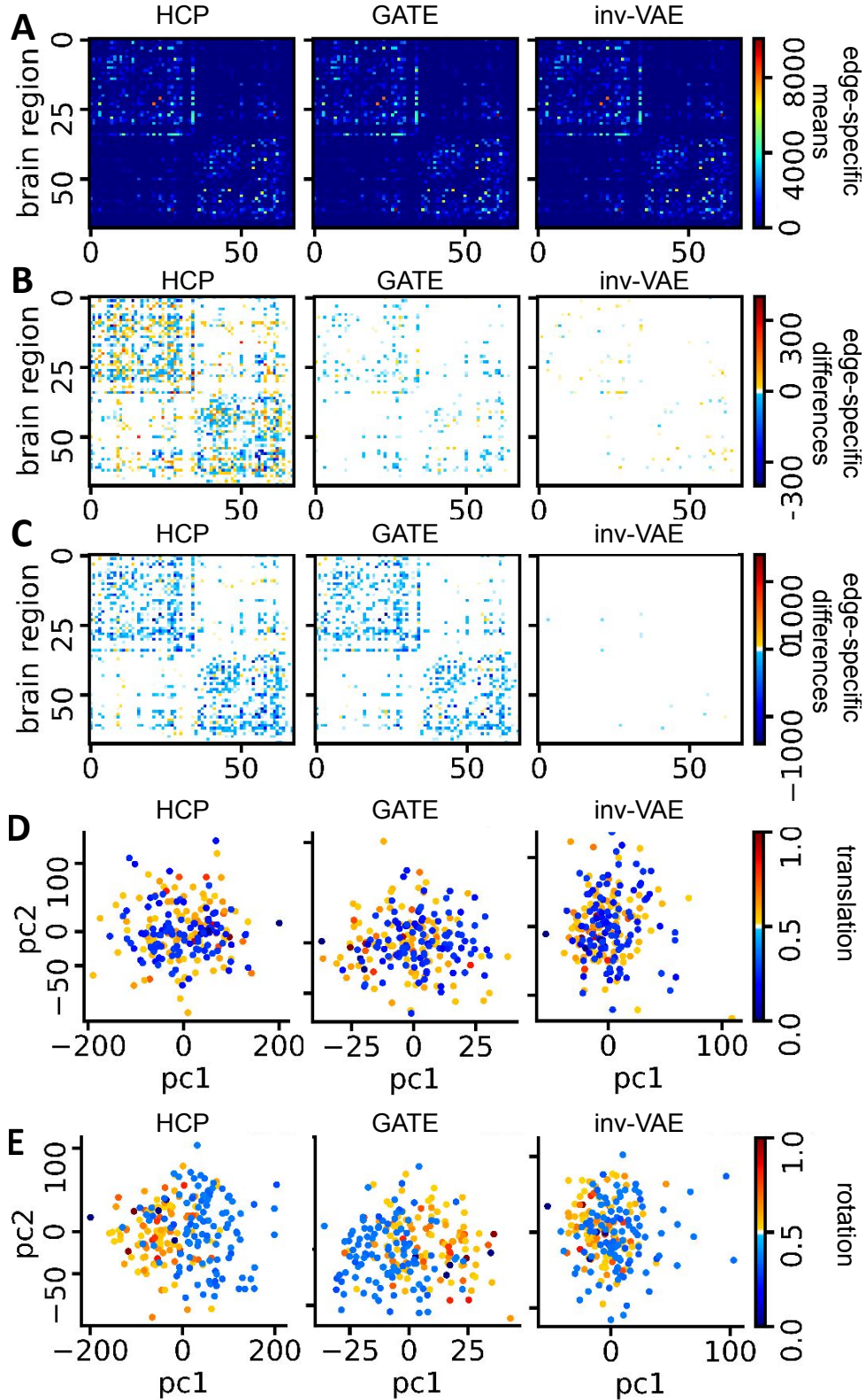


Figure 5: (A) From left to right: observed edge-specific means of HCP brain networks, reconstructed brain networks by GATE, and motion-adjusted brain networks by inv-VAE, color-coded by fiber count. (B) and (C): edge-specific differences (large group subtract small group) for translation and rotation respectively, colored by differences in fiber count. Ordering follows that in (A). (D) and (E): from left to right - the first two PC scores of HCP brain networks, latent embeddings learned by GATE, and invariant embeddings from inv-VAE for observations in the large and small-motion groups, colored by the amount of translation (D) and rotation (E) respectively.

small and a large motion group for each type of movement; See Section 2.2 for the cut-off thresholds for the large and small motion groups in both datasets. Fig. 4-5 (B, C) show the *motion-affected edge-specific differences*, obtained by subtracting the motion-affected edge-specific means of the small motion group from those of the large motion group. For both datasets, we notice apparent fiber count differences between the two motion groups in almost all pairs of brain regions. Such brain connection differences due to motion artifacts are more prominent when we visualized the first two PCs of brain networks between the two groups. In Fig. 4-5 (D, E), each point represents an individual colored with the corresponding amount of translation or rotation (standardized). In Fig. 5 (D, E), the PCA projections of the large and small motion subjects are closer compared to those in Fig. 4 (D, E). This may be explained by the amount of motion artifacts in the data: participants of the HCP study were young adults who may move less during data acquisition relative to the young adolescent ABCD participants.

Next, we applied GATE [31] to the ABCD and HCP data. For each dataset, GATE was trained using all brain networks \mathbf{A}_i 's to learn the model parameters θ and ϕ . Equipped with well-trained estimators, GATE obtained the learned latent variables from the inference model and reconstructed brain networks from the generative model in (12). We denote the *reconstructed brain network* as $\hat{\mathbf{A}}_i$. Fig. 4-5 (A) show the *reconstructed edge-specific means* averaged across all $\hat{\mathbf{A}}_i$'s in both datasets. In Fig. 4-5 (B, C), *reconstructed edge-specific differences* between the large and small translation and rotation group are shown. Although GATE can generate brain networks that resemble the observed data, motion artifacts were also undesirably reconstructed, as shown in Fig. 4-5 (B, C). The fact that GATE lacks the ability to adjust for motion is further evidenced by Fig. 4-5 (D, E), which show the first two PCs of the learned latents from the large and small motion group for each movement type. The gap between the two groups of latents suggests that representations learned by GATE are also corrupted by motion artifacts, which will further affect prediction and inferences.

For our inv-VAE, we use $\mathbf{c}_i = (c_{i1}, c_{i2}) \in \mathbb{R}^2$ to represent the i -th subject's motion, where c_{i1} and c_{i2} are the amount of translation and rotation, respectively. Both c_{i1} and c_{i2} were standardized so that 0 is the smallest amount of motion and 1 is the largest. To adjust for motion artifacts, we first trained the inv-VAE model using the ABCD and HCP data separately. The inference model of inv-VAE learned a set of motion-invariant representations \mathbf{z}_i . Following the generative model in Section 3.1, \mathbf{z}_i were subsequently used to generate *motion-adjusted brain networks*, denoted as \mathbf{A}_i^* , by setting \mathbf{c}_i to 0 to remove motion artifacts. For each dataset, we averaged across all \mathbf{A}_i^* to obtain the *motion-adjusted edge-specific means* shown in Fig. 4-5 (A), which resemble the observed edge-specific means. Fig. 4-5 (B, C) show the *motion-adjusted edge-specific differences* by taking the difference between the motion-adjusted edge-specific means of the large and small motion group for each movement type. Compared to the color scale of the observed between-group edge-specific differences, the colors of the motion-adjusted between-group edge-specific differences are noticeably lighter, suggesting that brain connection differences between

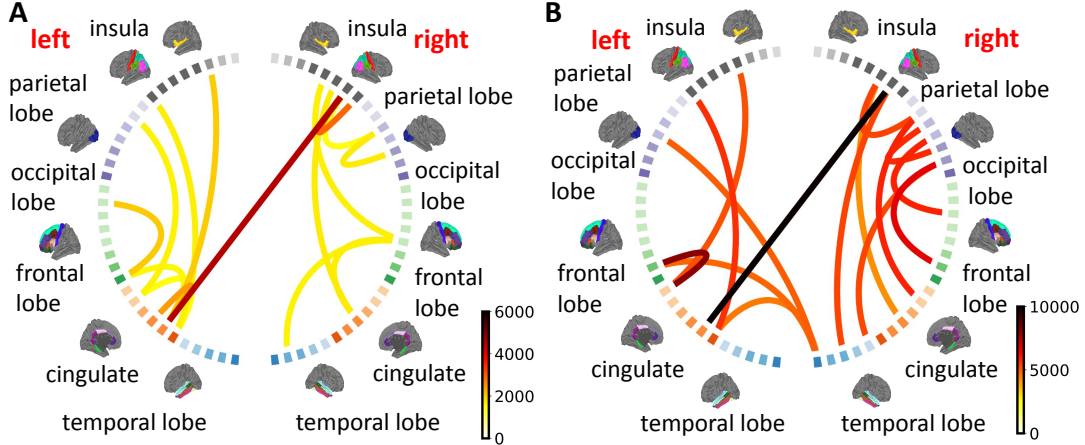


Figure 6: Structural connectivity differences between motion-adjusted and motion-affected ABCD (A) and HCP (B) brain networks; see Section 5.1 for definition. Each line connecting a pair of brain regions is colored by the corresponding fiber count difference after motion adjustment. We only show the 15 mostly changed brain connections.

the large and small motion groups become smaller after motion adjustment. Fig. 4-5 (D, E) show the first two PCs of invariant representations z_i for the ABCD and HCP data. The gap between large and small motion subjects is smaller after motion-adjustment compared to the projections of the observed brain networks. Although the HCP subjects have smaller head movement and their connectomes are less affected by motion artifacts, we still observe that motion-adjustment minimizes the reconstructed structural connection difference between the large and small motion group in Fig. 5 (B, C).

Next, we aim to understand how motion impacts our understanding of structural brain connectivity. For both ABCD and HCP studies, we first obtained the motion-affected edge-specific means via averaging A_i 's across all individuals in the dataset. After training inv-VAE using all A_i 's, we generated motion-adjusted networks A_i^* 's from the invariant embeddings. We then averaged across all A_i^* 's to construct the motion-adjusted edge-specific means. The differences between the motion-adjusted and motion-affected edge-specific means are shown in Fig. 6 (A, B). In both datasets, we observe more connections between the cingulate and the other brain regions in both hemispheres after motion adjustment, implying that brain connections related to the cingulate are more severely impacted by motion artifacts. There are also notable impacts in other regions, including the frontal, temporal, occipital, and parietal lobes, where we observe significant changes in connection strength after motion adjustment.

5.2 Relating Motion-Adjusted Connectomes to Cognition-Related Traits

Our method can effectively adjust motion artifacts in the connectome data. A natural question is whether motion-invariant representations further our understanding of the relationship between brain connectomes and cognition-related traits. From the ABCD dataset, we extracted the following cognitive traits as y_i : 1) picture vocabulary test score for language comprehension; 2) oral reading recognition test

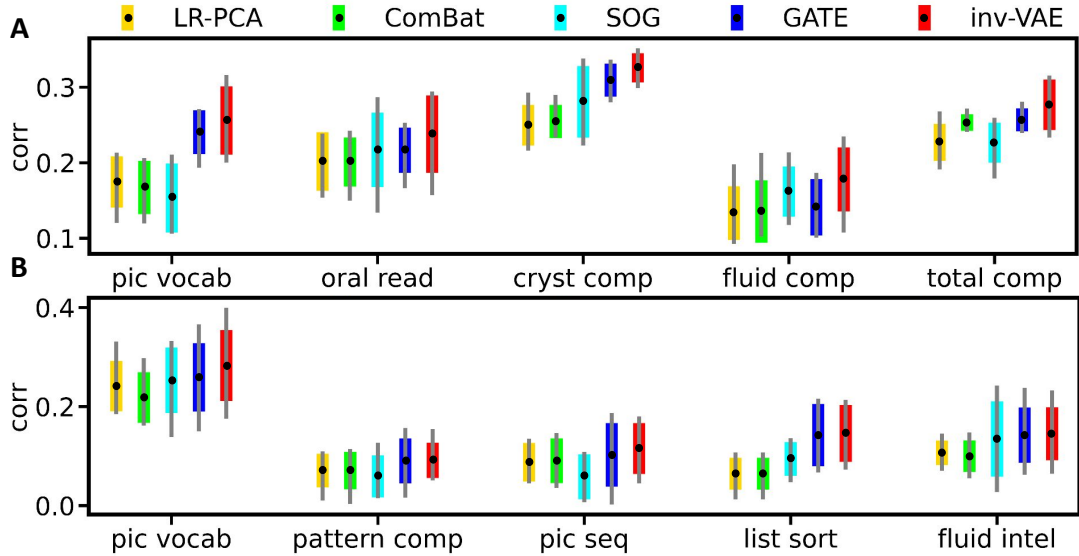


Figure 7: A comparison of all methods on trait prediction in the ABCD (A) and HCP (B) data. The error bars show the min, max, mean, and standard deviation of correlation coefficients from 5-fold CV.

score for language decoding; 3) fluid composite score for new learning; 4) crystallized composite score for past learning; 5) cognition total composite score for overall cognition capacity. From the HCP dataset, we considered similar traits: 1) picture vocabulary test score; 2) pattern completion test score for processing speed; 3) picture sequence test score for episodic memory; 4) list sorting test score for working memory; 5) fluid intelligence score; see [28] for details about these traits. All traits were age-corrected.

To investigate whether our method outperforms other approaches in relating structural connectomes to traits, we compared inv-VAE to the following competitors: 1) *LR-PCA* (motion-adjusted) uses PCA to obtain a lower-dimensional projection from each individual’s brain matrix, and then links y_i to the projection via a linear regression (LR). Translation and rotation are covariates that LR adjusts for. 2) *Sparse Orthogonal to Group (SOG)* [14] utilizes matrix decomposition to produce an adjusted dataset that is statistically independent of the motion variable. We then regress y_i onto the obtained low-dimensional factorizations via LR. 3) *ComBat* [16] uses empirical Bayes for batch-effect removal, and returns a motion-adjusted dataset. We then apply PCA to the adjusted data to obtain low-dimensional projections as input to LR. 4) *GATE* [31] has the same architecture as inv-VAE, but does not adjust for motion; see Section 4 for details about the model specification.

We use the competing methods to produce 68-dimensional connectome representations for each individual, consistent with the recommended latent dimension K in inv-VAE; see Section 3. To assess trait prediction quality, we used the Pearson correlation coefficient to measure correlation between the observed and predicted traits, and performed 5-fold cross-validation (CV). A large correlation coefficient means the predicted trait scores more closely match the observed ones, indicating a stronger association between the low-dimensional representations of structural connectomes and the cognition-related traits.

A comparison of inv-VAE to the other approaches w.r.t. the trait-prediction quality is displayed in

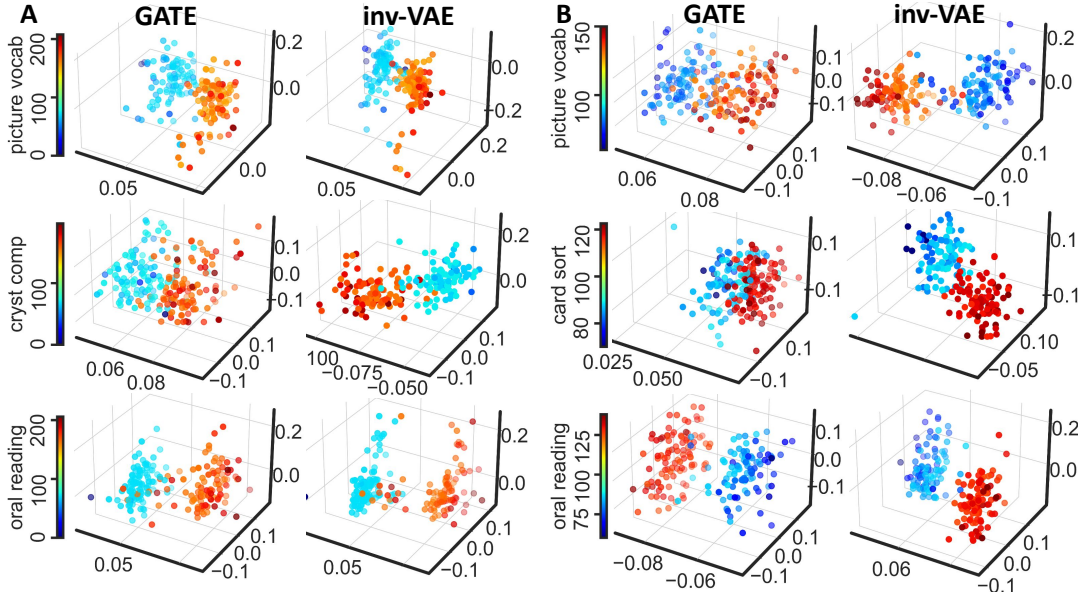


Figure 8: Relationships between learned embeddings and cognition-related traits in ABCD (**A**) and HCP (**B**) datasets. For each trait y_i , the first three PCs of the posterior means of z_i colored with their corresponding trait scores are displayed. Latent embeddings learned by GATE and motion-invariant embeddings from inv-VAE are compared.

Fig. 7, which shows that inv-VAE outperforms LR-PCA, ComBat and SOG over all studied traits in both datasets, and either outperforms or is comparable to GATE over most selected traits. As expected, given the tendency for larger head movement in the ABCD participants, inv-VAE performed better in ABCD compared with GATE. The prediction quality of SOG is comparable with GATE and inv-VAE for some cognitive traits: oral reading recognition and fluid intelligence score.

Another way to assess the predictive performance is to visualize the associations between low-dimensional representations of structural connectomes and cognition-related traits. Both inv-VAE and GATE produce latent features z_i for each individual, which can be used for visualizations. Particularly, for the ABCD study, we considered picture vocabulary test, oral reading recognition test and crystalized composite score; for the HCP study, we considered picture vocabulary test, oral reading recognition test and dimensional change card sort test. Both inv-VAE and GATE were trained with brain networks of all individuals in each dataset to obtain the z_i 's for the y_i 's. For each trait, latent features from 200 subjects were selected, with the first group of 100 having the lowest trait scores and the second group of 100 having the highest scores. Next, we plotted the first three PCs of the posterior means of z_i colored with their corresponding trait scores in Fig. 8. For both inv-VAE and GATE, Fig. 8 shows that representations from the two trait groups were separated, suggesting that structural connectomes are different among individuals with different cognitive abilities. We highlight that motion-invariant z_i 's of the two groups are more separated than motion-affected z_i 's from GATE, particularly for the oral reading recognition test. It implies that motion-invariant structural connectomes are more strongly associated with cognition-related traits than other approaches without motion adjustment.

6 Discussion

We developed a motion invariant variational auto-encoder (inv-VAE) for learning low-dimensional, motion-adjusted representations of structural connectomes. We applied inv-VAE to the Adolescent Brain Cognitive Development (ABCD) and Human Connectome Project (HCP) data and discovered noticeable motion artifacts in both, despite the incorporation of motion correction procedures in pre-processing. This observation reinforces the need for effective motion mitigation strategies in connectome analysis. Being invariant to motion artifacts during the connectome modeling phase, inv-VAE shows improved performance in understanding the correlation between structural connectomes and cognition-related traits. While our inv-VAE was motivated to handle the motion confounder, it can be easily extended to handle other confounders, such as site batch effect, variation due to machine settings, etc. Compared with popular batch effect removing models such as ComBat, the advantages of our inv-VAE include 1) it can handle non-linear objects (brain network data), and 2) it can deal with non-linear batch effects. Therefore, we believe that our inv-VAE framework can be extended to broader brain imaging analysis tasks, highlighting the importance of confounder or batch effect adjustment methodologies.

inv-VAE is developed under a generative model framework, which allows us to simulate brain networks under various conditions. The simulation of high-fidelity brain networks is crucial since brain network data are generally not widely available, and the extraction of brain networks from raw imaging data is far from straightforward. Our inv-VAE enables us to simulate (A_i, c_i, y_i) — that is, the brain network, motion artifacts, and cognition ability measures — simultaneously. Such simulated data can be freely shared with biostatisticians and data scientists who wish to develop statistical models for brain networks, but prefer not to get involved in the intricate process of brain imaging preprocessing.

Our proposed inv-VAE currently models the motion-affected structural connectome using a Poisson generative model in conjunction with a GCN. Future work could incorporate pre-existing neuroscience knowledge regarding the effects of motion artifacts on specific brain regions or connections to refine our model and improve the reconstruction of motion-adjusted structural connectomes. This could be achieved by leveraging empirical evidence, neuroscientific findings, or theoretical frameworks that shed light on the disparate impacts of motion artifacts on individual brain regions or connections. Through this integration of knowledge, we aim to boost the precision and accuracy of our motion artifact mitigation process, enabling us better to capture the subtle influences of motion on brain connectivity.

Another future direction is to leverage recent developments of generative modeling frameworks, such as variational diffusion models [37], score-based generative models [38] and Hierarchical Variational Autoencoders (HVAE) [36]. These models can be understood under the general Evidence Lower Bound (ELBO) method used here in this paper but with different constraints in the latent space [39]. Moreover, we used mean rotation and translation to represent motion during diffusion MRI acquisition and ignored the longitudinal or higher-order information in the motion. This simplification may not fully represent

the impacts of head motion on diffusion MRI data, and thus the motion-adjusted connectomes from our inv-VAE may not be completely invariant to motion. Future developments may incorporate more complex summaries of dynamic head motion.

References

- [1] Glasser, M.F., Smith, S.M., Marcus, D.S., Andersson, J.L., Auerbach, E.J., Behrens, T.E., Coalson, T.S., Harms, M.P., Jenkinson, M., Moeller, S. and Robinson, E.C., 2016. The human connectome project’s neuroimaging approach. *Nature Neuroscience*, 19(9), pp.1175-1187.
- [2] Bjork, J.M., Straub, L.K., Provost, R.G. and Neale, M.C., 2017. The ABCD study of neurodevelopment: Identifying neurocircuit targets for prevention and treatment of adolescent substance abuse. *Current Treatment Options in Psychiatry*, 4, pp.196-209.
- [3] Zhang, Z., Descoteaux, M., Zhang, J., Girard, G., Chamberland, M., Dunson, D., Srivastava, A. and Zhu, H., 2018. Mapping population-based structural connectomes. *NeuroImage*, 172, pp.130-145.
- [4] Zhang, Z., Allen, G.I., Zhu, H. and Dunson, D., 2019. Tensor network factorizations: Relationships between brain structural connectomes and traits. *NeuroImage*, 197, pp.330-343.
- [5] Andersson, J.L., Graham, M.S., Zsoldos, E. and Sotiropoulos, S.N., 2016. Incorporating outlier detection and replacement into a non-parametric framework for movement and distortion correction of diffusion MR images. *NeuroImage*, 141, pp.556-572.
- [6] Zemel, R., Wu, Y., Swersky, K., Pitassi, T. and Dwork, C., 2013. Learning fair representations. In *International Conference on Machine Learning* (pp. 325-333). PMLR.
- [7] Achille, A. and Soatto, S., 2018. Emergence of invariance and disentanglement in deep representations. *The Journal of Machine Learning Research*, 19(1), pp.1947-1980.
- [8] Kochunov, P., Lancaster, J.L., Glahn, D.C., Purdy, D., Laird, A.R., Gao, F. and Fox, P., 2006. Retrospective motion correction protocol for high-resolution anatomical MRI. *Human Brain Mapping*, 27(12), pp.957-962.
- [9] Bhushan, C., Halder, J.P., Choi, S., Joshi, A.A., Shattuck, D.W. and Leahy, R.M., 2015. Co-registration and distortion correction of diffusion and anatomical images based on inverse contrast normalization. *NeuroImage*, 115, pp.269-280.
- [10] Ben-Amitay, S., Jones, D.K. and Assaf, Y., 2012. Motion correction and registration of high b-value diffusion weighted images. *Magnetic Resonance in Medicine*, 67(6), pp.1694-1702.

- [11] Chang, L.C., Jones, D.K. and Pierpaoli, C., 2005. RESTORE: robust estimation of tensors by outlier rejection. *Magnetic Resonance in Medicine*, 53(5), pp.1088-1095.
- [12] Li, X., Yang, J., Gao, J., Luo, X., Zhou, Z., Hu, Y., Wu, E.X. and Wan, M., 2014. A robust post-processing workflow for datasets with motion artifacts in diffusion kurtosis imaging. *PloS One*, 9(4), p.e94592.
- [13] Alter, O., Brown, P.O. and Botstein, D., 2000. Singular value decomposition for genome-wide expression data processing and modeling. *Proceedings of the National Academy of Sciences*, 97(18), pp.10101-10106.
- [14] Aliverti, E., Lum, K., Johndrow, J.E. and Dunson, D.B., 2021. Removing the influence of group variables in high-dimensional predictive modelling. *Journal of the Royal Statistical Society. Series A, (Statistics in Society)*, 184(3), p.791.
- [15] Benito, M., Parker, J., Du, Q., Wu, J., Xiang, D., Perou, C.M. and Marron, J.S., 2004. Adjustment of systematic microarray data biases. *Bioinformatics*, 20(1), pp.105-114.
- [16] Johnson, W.E., Li, C. and Rabinovic, A., 2007. Adjusting batch effects in microarray expression data using empirical Bayes methods. *Biostatistics*, 8(1), pp.118-127.
- [17] Duffy, B.A., Zhang, W., Tang, H., Zhao, L., Law, M., Toga, A.W. and Kim, H., 2018. Retrospective correction of motion artifact affected structural MRI images using deep learning of simulated motion. In *Medical Imaging with Deep Learning*.
- [18] Lample, G., Zeghidour, N., Usunier, N., Bordes, A., Denoyer, L. and Ranzato, M.A., 2017. Fader networks: Manipulating images by sliding attributes. *Advances in Neural Information Processing Systems*, 30.
- [19] Zhang, H., Chen, H., Song, Z., Boning, D., Dhillon, I.S. and Hsieh, C.J., 2019. The limitations of adversarial training and the blind-spot attack. *The International Conference on Learning Representations*, 7.
- [20] Moyer, D., Gao, S., Brekelmans, R., Galstyan, A. and Ver Steeg, G., 2018. Invariant representations without adversarial training. *Advances in Neural Information Processing Systems*, 31.
- [21] Andersson, J.L. and Sotiropoulos, S.N., 2016. An integrated approach to correction for off-resonance effects and subject movement in diffusion MR imaging. *NeuroImage*, 125, pp.1063-1078.
- [22] Casey, B.J., Cannonier, T., Conley, M.I., Cohen, A.O., Barch, D.M., Heitzeg, M.M., Soules, M.E., Teslovich, T., Dellarco, D.V., Garavan, H. and Orr, C.A., 2018. The adolescent brain cognitive development (ABCD) study: imaging acquisition across 21 sites. *Developmental Cognitive Neuroscience*, 32, pp.43-54.

- [23] Van Essen, D.C., Ugurbil, K., Auerbach, E., Barch, D., Behrens, T.E., Bucholz, R., Chang, A., Chen, L., Corbetta, M., Curtiss, S.W. and Della Penna, S., 2012. The Human Connectome Project: a data acquisition perspective. *NeuroImage*, 62(4), pp.2222-2231.
- [24] Maier-Hein, K.H., Neher, P.F., Houde, J.C., Côté, M.A., Garyfallidis, E., Zhong, J., Chamberland, M., Yeh, F.C., Lin, Y.C., Ji, Q. and Reddick, W.E., 2017. The challenge of mapping the human connectome based on diffusion tractography. *Nature Communications*, 8(1), p.1349.
- [25] Desikan, R.S., Ségonne, F., Fischl, B., Quinn, B.T., Dickerson, B.C., Blacker, D., Buckner, R.L., Dale, A.M., Maguire, R.P., Hyman, B.T. and Albert, M.S., 2006. An automated labeling system for subdividing the human cerebral cortex on MRI scans into gyral based regions of interest. *NeuroImage*, 31(3), pp.968-980.
- [26] Iannopollo, E., Plunkett, R. and Garcia, K., 2019. Surface-based analysis of cortical thickness and volume loss in Alzheimer’s disease. *Proceedings of the International Max Planck Research Schools*, 2(1).
- [27] Fornito, A., Zalesky, A. and Breakspear, M., 2013. Graph analysis of the human connectome: promise, progress, and pitfalls. *NeuroImage*, 80, pp.426-444.
- [28] Gershon, R.C., Wagster, M.V., Hendrie, H.C., Fox, N.A., Cook, K.F. and Nowinski, C.J., 2013. NIH toolbox for assessment of neurological and behavioral function. *Neurology*, 80 (11 Supplement 3), pp.S2-S6.
- [29] Kingma, D.P. and Welling, M., 2013. Auto-encoding variational Bayes. *arXiv:1312.6114*.
- [30] Hoff, P.D., Raftery, A.E. and Handcock, M.S., 2002. Latent space approaches to social network analysis. *Journal of the American Statistical Association*, 97(460), pp.1090-1098.
- [31] Liu, M., Zhang, Z. and Dunson, D.B., 2021. Graph auto-encoding brain networks with applications to analyzing large-scale brain imaging datasets. *NeuroImage*, 245, p.118750.
- [32] Haller, S., Monsch, A.U., Richiardi, J., Barkhof, F., Kressig, R.W. and Radue, E.W., 2014. Head motion parameters in fMRI differ between patients with mild cognitive impairment and Alzheimer disease versus elderly control subjects. *Brain Topography*, 27, pp.801-807.
- [33] Nowicki, K. and Snijders, T.A.B., 2001. Estimation and prediction for stochastic blockstructures. *Journal of the American Statistical Association*, 96(455), pp.1077-1087.
- [34] Louizos, C., Swersky, K., Li, Y., Welling, M. and Zemel, R., 2015. The variational fair autoencoder. *The International Conference on Learning Representations*, 4.
- [35] Kingma, D.P. and Ba, J., 2014. Adam: A method for stochastic optimization. *arXiv:1412.6980*.

- [36] Sønderby, C.K., Raiko, T., Maaløe, L., Sønderby, S.K., and Winther, O., 2016. Ladder variational autoencoders. *Advances in Neural Information Processing Systems*, vol. 29.
- [37] Kingma, D., Salimans, T., Poole, B., and Ho, J., 2021. Variational diffusion models. *Advances in Neural Information Processing Systems*, vol. 34, pp. 21696-21707.
- [38] Song, Y., and Ermon, S., 2020. Improved techniques for training score-based generative models. *Advances in Neural Information Processing Systems*, vol. 33, pp. 12438-12448.
- [39] Luo, C., 2022. Understanding diffusion models: A unified perspective. *arXiv:2208.11970*.

APPENDIX

A. GCN model specification

To exploit the local collaborative patterns among brain regions, [31] proposed to learn each region’s representation by propagating node-specific k -nearest neighbor information. We use the relative distance between a pair of brain regions to represent their locality. The relative distance is measured through the length of the white matter fiber tract connecting the pair, and stored in a matrix $\mathbf{D} \in \mathbb{R}^{V \times V}$. D_{uv} denotes the fiber length between regions u and v . For u , its k -nearest neighbors (kNNs) can be defined according to \mathbf{D} . Graph convolution is defined to learn the r -th latent coordinate $\mathbf{X}_r(\tilde{\mathbf{z}}_i)$ for subject i . In particular, an m -layer GCN is $\mathbf{X}_r^{(m)}(\tilde{\mathbf{z}}_i) = h_m(\mathbf{W}_r^{(m)} \mathbf{X}_r^{(m-1)}(\tilde{\mathbf{z}}_i) + b_m)$, for $2 \leq m \leq M$, with $\mathbf{X}_r^{(1)}(\tilde{\mathbf{z}}_i) = h_1(\mathbf{W}_r^{(1)} \tilde{\mathbf{z}}_i + b_1)$. $\mathbf{X}_r^{(m)}(\tilde{\mathbf{z}}_i)$ denotes the output of the m -th GCN layer, $h_m(\cdot)$ is an activation function of the m -th layer, and $\mathbf{W}_r^{(m)}$ is a weight matrix characterizing the convolution operation at the m -th layer. The embedding feature of each region at the m -th layer is determined by the weighted sum of itself and its nearest neighbor regions at the $(m-1)$ -th layer. When $m=1$, $\mathbf{W}_r^{(1)} \in \mathbb{R}^{V \times (K+C)}$ maps $\tilde{\mathbf{z}}_i \in \mathbb{R}^{K+C}$ to the latent space $\mathbf{X}_r^{(1)}(\tilde{\mathbf{z}}_i) \in \mathbb{R}^V$. When $m \geq 2$, $\mathbf{W}_r^{(m)}$ is a $V \times V$ matrix with the u -th row $\mathbf{w}_u^{(r,m)}$ satisfying $w_{uv}^{(r,m)} > 0$ if $v = u$ or $v \in k_r\text{NN}(u)$, and $w_{uv}^{(r,m)} = 0$ otherwise.

B. Derivation of the joint likelihood of \mathbf{A}_i, y_i conditional on \mathbf{c}_i defined in (8)

The joint likelihood of \mathbf{A}_i and y_i given \mathbf{c}_i is

$$\log p_{\theta}(\mathbf{A}_i, y_i | \mathbf{c}_i) = \log \left(\int \frac{p_{\theta}(\mathbf{A}_i, y_i, \mathbf{z}_i | \mathbf{c}_i)}{q_{\phi}(\mathbf{z}_i | \mathbf{A}_i)} q_{\phi}(\mathbf{z}_i | \mathbf{A}_i) d\mathbf{z}_i \right) = \log \left(\mathbb{E}_{\mathbf{z}_i \sim q_{\phi}} \left[\frac{p_{\theta}(\mathbf{A}_i, y_i, \mathbf{z}_i | \mathbf{c}_i)}{q_{\phi}(\mathbf{z}_i | \mathbf{A}_i)} \right] \right).$$

By Jensen’s inequality,

$$\begin{aligned} \log \left(\mathbb{E}_{\mathbf{z}_i \sim q_{\phi}} \left[\frac{p_{\theta}(\mathbf{A}_i, y_i, \mathbf{z}_i | \mathbf{c}_i)}{q_{\phi}(\mathbf{z}_i | \mathbf{A}_i)} \right] \right) &\geq \mathbb{E}_{\mathbf{z}_i \sim q_{\phi}} [\log p_{\theta}(\mathbf{A}_i, y_i, \mathbf{z}_i | \mathbf{c}_i) - \log q_{\phi}(\mathbf{z}_i | \mathbf{A}_i)] \\ &= \mathbb{E}_{\mathbf{z}_i \sim q_{\phi}} [\log p_{\theta}(\mathbf{A}_i, y_i | \mathbf{z}_i, \mathbf{c}_i) + \log p_{\theta}(\mathbf{z}_i | \mathbf{c}_i) - \log q_{\phi}(\mathbf{z}_i | \mathbf{A}_i)]. \end{aligned}$$

Assuming that \mathbf{z}_i is independent of \mathbf{c}_i , we have $p_{\theta}(\mathbf{z}_i | \mathbf{c}_i) = p(\mathbf{z}_i)$. We then have

$$\begin{aligned} & \mathbb{E}_{\mathbf{z}_i \sim q_{\phi}}[\log p_{\theta}(\mathbf{A}_i, y_i | \mathbf{z}_i, \mathbf{c}_i)] + \mathbb{E}_{\mathbf{z}_i \sim q_{\phi}}[\log p_{\theta}(\mathbf{z}_i) - \log q_{\phi}(\mathbf{z}_i | \mathbf{A}_i)] \\ &= \mathbb{E}_{\mathbf{z}_i \sim q_{\phi}}[\log p_{\theta}(\mathbf{A}_i, y_i | \mathbf{z}_i, \mathbf{c}_i)] - KL[q_{\phi}(\mathbf{z}_i | \mathbf{A}_i) || p(\mathbf{z}_i)]. \end{aligned}$$

C. Derivation of mutual information $I(\mathbf{z}_i, \mathbf{c}_i)$ defined in (7)

From mutual information properties, we have that

$$I(\mathbf{z}_i, \mathbf{c}_i) = I(\mathbf{z}_i, \mathbf{A}_i) - I(\mathbf{z}_i, \mathbf{A}_i | \mathbf{c}_i) + I(\mathbf{z}_i, \mathbf{c}_i | \mathbf{A}_i),$$

where

$$I(\mathbf{z}_i, \mathbf{c}_i | \mathbf{A}_i) = H(\mathbf{z}_i | \mathbf{A}_i) - H(\mathbf{z}_i | \mathbf{A}_i, \mathbf{c}_i) = H(\mathbf{z}_i | \mathbf{A}_i) - H(\mathbf{z}_i | \mathbf{A}_i) = 0,$$

because the distribution of \mathbf{z}_i solely depends on \mathbf{A}_i not on \mathbf{c}_i . Using mutual information properties, we write $I(\mathbf{z}_i, \mathbf{c}_i)$ as

$$I(\mathbf{z}_i, \mathbf{c}_i) = I(\mathbf{z}_i, \mathbf{A}_i) - I(\mathbf{z}_i, \mathbf{A}_i | \mathbf{c}_i) = I(\mathbf{z}_i, \mathbf{A}_i) - H(\mathbf{A}_i | \mathbf{c}_i) + H(\mathbf{A}_i | \mathbf{z}_i, \mathbf{c}_i).$$

Using variational inequality, we have

$$\begin{aligned} I(\mathbf{z}_i, \mathbf{c}_i) &\leq I(\mathbf{z}_i, \mathbf{A}_i) - H(\mathbf{A}_i | \mathbf{c}_i) - \mathbb{E}_{\mathbf{A}_i, \mathbf{z}_i, \mathbf{c}_i \sim q_{\phi}}[\log p_{\theta}(\mathbf{A}_i | \mathbf{z}_i, \mathbf{c}_i)] \\ &= \mathbb{E}_{\mathbf{z}_i, \mathbf{A}_i}[\log q_{\phi}(\mathbf{z}_i | \mathbf{A}_i) - \log q_{\phi}(\mathbf{z}_i)] - H(\mathbf{A}_i | \mathbf{c}_i) - \mathbb{E}_{\mathbf{A}_i, \mathbf{c}_i, \mathbf{z}_i \sim q_{\phi}}[\log p_{\theta}(\mathbf{A}_i | \mathbf{z}_i, \mathbf{c}_i)] \\ &= \mathbb{E}_{\mathbf{A}_i}[KL[q_{\phi}(\mathbf{z}_i | \mathbf{A}_i) || q_{\phi}(\mathbf{z}_i)]] - H(\mathbf{A}_i | \mathbf{c}_i) - \mathbb{E}_{\mathbf{A}_i, \mathbf{c}_i, \mathbf{z}_i \sim q_{\phi}}[\log p_{\theta}(\mathbf{A}_i | \mathbf{z}_i, \mathbf{c}_i)], \end{aligned}$$

where $H(\mathbf{A}_i | \mathbf{c}_i)$ is a constant that can be ignored.

D. Monte Carlo approximation of inv-VAE objective

We use Monte Carlo variational inference [29] to approximate the intractable expectation in our invariant objective. Using reparametrization trick, for each $\ell = 1, \dots, L$, we sample $\mathbf{z}_i^{\ell} \sim q_{\phi}(\mathbf{z}_i | \mathbf{A}_i) = \mathcal{N}(\boldsymbol{\mu}_{\phi}(\mathbf{A}_i), \boldsymbol{\Sigma}_{\phi}(\mathbf{A}_i))$, where $\boldsymbol{\mu}_{\phi}(\mathbf{A}_i) \in \mathbb{R}^K$ and $\boldsymbol{\Sigma}_{\phi}(\mathbf{A}_i) \in \mathbb{R}^{K \times K}$. With \mathbf{z}_i^{ℓ} , we decompose the objective in (10) into three parts: 1) The reconstruction error

$$\mathcal{L}_{\text{recon}} = \mathbb{E}_{\mathbf{z}_i \sim q_{\phi}}[\log p_{\theta}(\mathbf{A}_i | \mathbf{z}_i, \mathbf{c}_i) + \log p_{\theta}(y_i | \mathbf{z}_i)]$$

can be approximated by $\tilde{\mathcal{L}}_{\text{recon}} = \frac{1}{L} \sum_{\ell=1}^L (\log p_{\theta}(\mathbf{A}_i | \mathbf{z}_i^{\ell}, \mathbf{c}_i) + \log p_{\theta}(y_i | \mathbf{z}_i^{\ell}))$. 2) Because both $q_{\phi}(\mathbf{z}_i | \mathbf{A}_i)$ and $p_{\theta}(\mathbf{z}_i)$ are normally distributed, the KL divergence between them,

$$\mathcal{L}_{\text{prior}} = KL \left[q_{\phi}(\mathbf{z}_i | \mathbf{A}_i) \parallel p(\mathbf{z}_i) \right],$$

can be approximated by $\tilde{\mathcal{L}}_{\text{prior}} = \frac{1}{2} \sum_{k=1}^K (\mu_k^2 + \sigma_k^2 - 1 - \log(\sigma_k^2))$, where μ_k, σ_k are the k -th element of $\boldsymbol{\mu}_{\phi}(\mathbf{A}_i)$ and $\boldsymbol{\Sigma}_{\phi}(\mathbf{A}_i)$. 3) $q_{\phi}(\mathbf{z}_i)$ is the marginal distribution of $q_{\phi}(\mathbf{z}_i | \mathbf{A}_i)$, and they are two Gaussians. We can approximate

$$\mathcal{L}_{\text{marg}} = KL[q_{\phi}(\mathbf{z}_i | \mathbf{A}_i) \parallel q_{\phi}(\mathbf{z}_i)]$$

with the following pairwise Gaussian KL divergence [34]:

$$\tilde{\mathcal{L}}_{\text{marg}} = KL[q_{\phi}(\mathbf{z}_i | \mathbf{A}_i) \parallel q_{\phi}(\mathbf{z}_i)] = \frac{1}{2} \left[\log \frac{\det(\boldsymbol{\Sigma}_0)}{\det(\boldsymbol{\Sigma}_1)} + \text{tr}(\boldsymbol{\Sigma}_0^{-1} \boldsymbol{\Sigma}_1) - K + (\boldsymbol{\mu}_0 - \boldsymbol{\mu}_1)^{\top} \boldsymbol{\Sigma}_1^{-1} (\boldsymbol{\mu}_0 - \boldsymbol{\mu}_1) \right],$$

where $\boldsymbol{\mu}_0$ and $\boldsymbol{\Sigma}_0$ parametrize $q_{\phi}(\mathbf{z}_i)$, and $\boldsymbol{\mu}_1$ and $\boldsymbol{\Sigma}_1$ parametrize $q_{\phi}(\mathbf{z}_i | \mathbf{A}_i)$. The approximated invariant objective, $\tilde{\mathcal{L}}(\mathbf{A}_i, y_i, \mathbf{c}_i; \boldsymbol{\theta}, \phi) = (1 + \lambda)\tilde{\mathcal{L}}_{\text{recon}} - \lambda\tilde{\mathcal{L}}_{\text{marg}} - \tilde{\mathcal{L}}_{\text{prior}}$, is now differentiable w.r.t. $\boldsymbol{\theta}$ and ϕ .

E. More on experiments

The architecture of our inv-VAE is presented in Table 1. Cross-validation was employed to select the model parameters that optimize performance based on the specified loss function. The latent dimension size and network depth were chosen to achieve the minimal training loss. We used the Adam optimizer [35] to train both inv-VAE and GATE on a GPU device. During model training, the parameters in Table 1 were set to be the same for both inv-VAE and GATE for a fair comparison. The learning rate was set to $5e^{-6}$ in the simulation study and $2e^{-5}$ in applications to the two datasets. For the mini-batches, we chose a batch size of 32, and the batches were sampled uniformly at random at each epoch and repeated for 200 epochs in both simulation study and real applications.

Table 1: Model architecture of inv-VAE.

	Inference Model (Encoder)	Generative Model (Decoder)
inv-VAE	$\mathbf{W}_1 : 68 \times 256$	k -NN: 32
	$\mathbf{W}_2 : 256 \times 68$	$K = 68$
	$b_1 : 256 \times 1$	$M = 2$
	$b_2 : 68 \times 1$	$R = 5$
	φ_1 : ReLU	h_1 : Sigmoid
	φ_2 : Linear	h_2 : Sigmoid

K is the latent dimension of \mathbf{z}_i ; M is the number of GCN layers; R is the latent dimension of $\mathbf{X}(\tilde{\mathbf{z}}_i)$; \mathbf{W}, b, φ . are weights, biases and activation functions in the encoder; h . are the activation functions in the decoder.